RESEARCH ARTICLE

Editor's Choice

ADVANCED ENERGY MATERIALS

www.advenergymat.de

# Laterally $\pi$-Extensed Nitrogen-Doped Molecular Nanographenes – From Anti-Kasha Emission to Ping-Pong Energy Transfer Events

*Giovanni M. Beneventi, Kilian Schöll, Benedikt Platzer, Marcel Krug, Lukas A. Mai, Fabrizia Negri, Alejandro Cadranel, Norbert Jux,* and Dirk M. Guldi**

**Nanographenes, which feature at least one dimension smaller than 100 nm, are drawing interdisciplinary attention. Understanding the interplay between structure and properties is, however, still in its infancy. Molecular nanographenes are much better suited to fill this knowledge gap than graphene quantum dots or nanoribbons. Their bottom-up synthesis allows atomic precision and, thereby, assists in handling structure and connecting it with properties. Herein, the effects of nitrogen-doping and lateral $\pi$-extension in molecular nanographenes and in their coordination complexes with ruthenium porphyrins are investigated. The presence of just nitrogen resulted in an increase of the fluorescence quantum yield, without, however, affecting the energy levels. Lateral $\pi$-extension of the nanographenes, instead, resulted in a modulation of the excited states energy, which leads to a thermally-activated dual fluorescence with quantum yields as high as 61%. In the corresponding coordination complexes, lateral $\pi$-extension resulted in a ping-pong energy transfer cascade, that is, from the nanographene to the metalloporphyrin and back to the nanographene. The results help to directly rationalize properties observed in both graphene quantum dots and nanoribbons. Moreover, they prove that molecular nanographenes are appealing components for solar energy conversion schemes, where the modulation of inter-component energy transfer is of utmost importance.**

## 1. Introduction

Nanographenes, namely sections of graphene with at least one dimension smaller than 100 nm, are on the rise in materials science.[1–3] Macroscopic graphene lacks a band gap. However, decreasing its lateral size to the nanodomain induces an opening of a gap in the band structure.[4,5] The latter aspect is fundamental when considering applications in fields such as optoelectronics and organic electronics.[1,6,7] Likewise, nanographenes stand out thanks to the ease, by which structural modifications enable modulation of the bandgap and beyond.[8–10]

There are three different subcategories in which nanographenes are generally sorted, that is, quantum dots, nanoribbons, and molecular nanographenes.[1] Quantum dots and nanoribbons generally lack exact and definable structures. As a matter of fact, quantum dots feature irregular structures, contain

G. M. Beneventi, B. Platzer, M. Krug, L. A. Mai, A. Cadranel, D. M. Guldi
Department of Chemistry and Pharmacy & Interdisciplinary Center for Molecular Materials (ICMM)
Friedrich-Alexander-University Erlangen-Nuremberg
Egerlandstraße 3, 91058 Erlangen, Germany
E-mail: dirk.guldi@fau.de

K. Schöll, N. Jux
Department of Chemistry and Pharmacy & Interdisciplinary Center for Molecular Materials (ICMM)
Friedrich-Alexander-University Erlangen-Nuremberg
Nikolaus-Fiebiger-Strasse 10, 91058 Erlangen, Germany
E-mail: norbert.jux@fau.de

The ORCID identification number(s) for the author(s) of this article can be found under https://doi.org/10.1002/aenm.202401529



**DOI: 10.1002/aenm.202401529**

F. Negri
Department of Chemistry "Giacomo Ciamician"
University of Bologna
Via Piero Gobetti 85, Bologna 40129, Italy

A. Cadranel
Facultad de Ciencias Exactas y Naturales
Departamento de Química Inorgánica
Analítica y Química Física
Universidad de Buenos Aires
Ciudad Universitaria
Pabellón 2, Buenos Aires C1428EHA, Argentina

A. Cadranel
CONICET – Universidad de Buenos Aires
Instituto de Química-Física de Materiales
Medio Ambiente y Energía (INQUIMAE)
Ciudad Universitaria
Pabellón 2, Buenos Aires C1428EHA, Argentina

defects, and/or are of undefined length and width.[1] Concerning nanoribbons, classic synthetic approaches generally allow control over edges and width, while attaining a defined length is quite challenging.[11–13] The latter is likely to affect the properties of the resulting nanoribbons, even if this effect is generally overlooked.[11,14] In stark contrast, molecular nanographenes feature a precisely determinable structure. They are synthesized via bottom-up approaches, such as wet-chemical or on-surface strategies, to allow atomic precision.[8,15–17] Amongst all, this subcategory is closest to the world of molecular materials than the one of macroscopic graphene, and a more suitable denominator for molecular nanographene is arguably (ultra)large polycyclic aromatic hydrocarbons (PAHs). To this end, one of the best-studied molecular nanographenes is hexa-perihexabenzocoronene (HBC). Its soluble derivatives have been known for more than half a century.[18–21]

Albeit being more difficult and perhaps less prone to high-throughput approaches, the synthesis of molecular nanographene is invaluable in terms of controlling atomic precision and essential in the context of understanding and rationalizing materials' properties. Undoubtedly, parameters such as length, width, edge structure, heteroatom doping, defects, functionality, etc. are likely to affect energy levels and edge states.[9,10] Any of the aforementioned parameters are crucial in impacting the optoelectronic, redox, as well as magnetic properties of nanographenes. For example, several cutting-edge effects have been showcased in applications with graphene quantum dots, but the lack of insights into their structure renders a general understanding rather difficult.[22–25] Concerning nanoribbons, their length is generally uncontrollable by any conventional synthetic protocols. This rationalizes the fact that photophysical studies with a focus on length and/or width dependence are scarce. Recent investigations demonstrated that nanoribbons are best described as large solvated organic molecules, rather than quantum-confined solids, as a result of strongly-.bound exciton transitions.[26–28] This validates per se the use of molecular nanographenes as a model for gathering a sound understanding of graphene nanoribbons. Importantly, a comprehensive approach to relating structure to the function of nanographene is the grand challenge in the field, as it is a necessity in meeting those requirements that are indispensable for a broad palette of applications.

Recent advances in the synthesis of molecular nanographenes are trendsetting, yet next to their chemical also their physical properties are poorly understood. Among others, solubility imposes great challenges to their characterization, especially when increasing the size of molecular nanographenes.[29] This calls for the need to control aggregation, which starts with understanding it. Photophysics, for example, is heavily impacted by any aggregation – static or dynamic. Overcoming and addressing such challenges is the true bottleneck in further advancing the fields.[30–35]

Nitrogen-doping of graphene and nanographene has attracted a lot of attention.[36–40] A leading example is nitrogen-doped graphene quantum dots.[41,42] It has been shown that graphitic nitrogen doping, at the core of aromatic domains, mainly increases emission quantum yields. Instead, pyridinic nitrogen doping, at the edge of aromatic domains, is photobasic and enables charge separation and enhanced photocatalytic hydrogen production from water, at the expense of emission.[43,44] Once again, a full understanding of the effect of nitrogen doping on the photophysical properties of both quantum dots and nanoribbons has not been achieved yet.[42,45,46]

To study the effect of nitrogen-doping in molecular nanographenes, we developed a series of nitrogen-doped molecular nanographenes. Azananographene **1** differs from **HBC** just by the presence of one nitrogen at one peripheral position (**Figure 1**). Additionally, the synthesis of a lateral $\pi$-extended diazananographene with two nitrogen atoms was achieved, namely **2**. Having the same edge structure and the same width as **HBC** and **1**, but a different length, **2** allowed us to investigate the influence of lateral extension on general photophysics. Additionally, the nitrogen presence at the peripheral positions allowed for the coordination of ruthenium porphyrin, leading to **RuP-1** and **RuP-2-RuP**.

We were able to substantiate that the nitrogen presence influences the optoelectronic features, in general, and the fluorescence quantum yields, in particular. Quite impactful was the effect of the lateral $\pi$-extension on the energy of both singlet and triplet excited states. Even if similar structures have been already reported, with and without nitrogen, the lack of knowledge on their state of aggregation hindered any in-depth studies.[28,47,48] We tackled this aspect via concentration-dependent analyses down to nanomolar concentrations, where the aggregation is largely suppressed. By supporting our experimental findings with cutting-edge quantum mechanical calculations, we demonstrated an efficient anti-Kasha emission in **2**. Lateral $\pi$-extension affected also the deactivation mechanism in **RuP-2-RuP**, when compared to that of **RuP-1** and other previously reported nanographene-porphyrin conjugates.[9,49–54] In particular, **RuP-2-RuP** undergoes a ping-pong energy transfer cascade upon photoexcitation, namely from **2** to **RuP** and back to **2**. Our results provide basic insights into the photophysics of molecular nanographenes, which will aid in rationalizing the features of much larger and structurally more diverse graphene nanoribbons.[27,28] Additionally, our findings highlight the great potential of nitrogen doping of nanographene.

The cascades of energy and electron transfer reactions are of uttermost importance in, for example, the light-harvesting machinery and photosynthetic reaction center, respectively.[55,56] It is the synergy of capturing light, transferring excitation energy, and dislocating charge carriers that assist in optimizing the conversion into chemical energy. To this end, controlling and regulating photochemical processes is at the forefront to maintain optimal performance under limiting light and minimize photodamage under excess light. We consider energy ping-pong processes as one potential approach to (down)regulate excitation energy.[57–60]

## 2. Results

### 2.1. Synthesis and Characterization

#### *2.1.1. Molecular Nanographenes*

Even though the core structure of diazananographene **2** has already been described,[61] we developed an alternative synthesis route (**Scheme 1**). *n*-Dodecyl chains were introduced in the bay positions to enhance solubility. The synthetic approach relies on the boron-masking strategy by Suginome, where

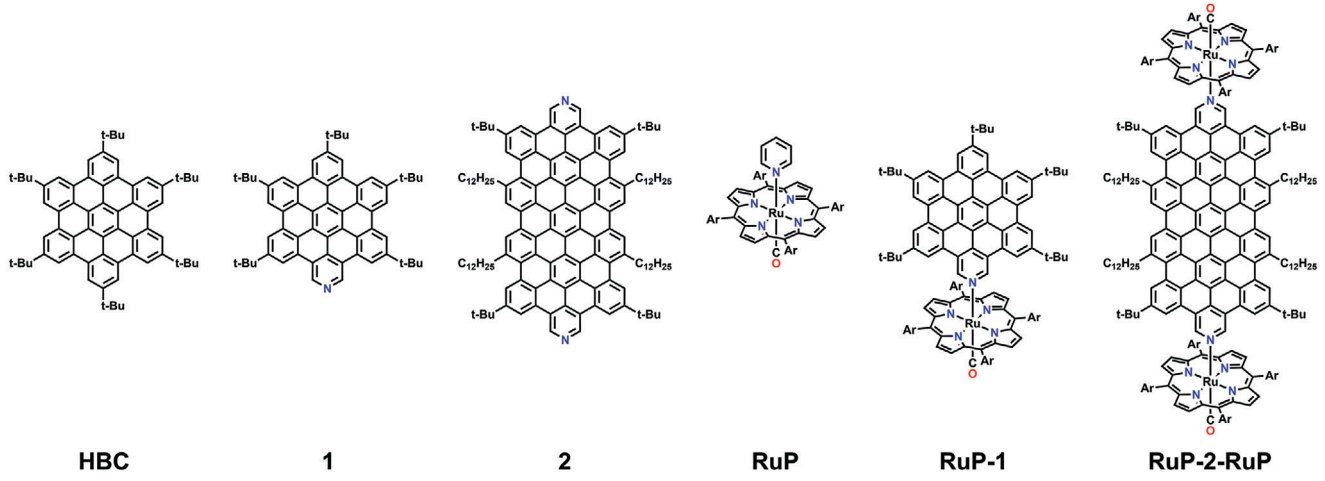


**Figure 1.** Chemical structures of the compounds studied herein. Ar: 3,5-di-tert-butylphenyl.

one-sidedly protected diboronic acid **4** enables a sequential Suzuki coupling.[62,63] The first coupling was carried out with **3**,[64] followed by an acid-catalyzed exchange of the diaminonaphthalene protection group with pinacol.[65] **6** was then coupled twice with **7**[66] to afford **8**. The second coupling reacted slowly, which necessitated a temperature of 100 °C. Still, 10 days were required to obtain **8** in a good yield of 73%. Planarization was achieved in one final step via oxidative cyclodehydrogenation under Scholl conditions. Polyphenylene **8** features pre-formed bonds in the 3/3′-positions of the pyridine ring that would otherwise be unreactive in the Scholl reaction, as demonstrated in our previous work.[64] Diazananographene **2** turned out to be quite insoluble at room temperature but readily dissolved in hot organic solvents (toluene, *o*-DCB, 1,1,2,2 tetrachloroethane). This allowed a facile workup procedure by filtration and recrystallization.

#### *2.1.2. Coordination Compounds*

Ruthenium carbonyl porphyrin **10** was prepared by metalation of the free base porphyrin with $Ru_3(CO)_{12}$ according to a modified literature procedure.[67] Meso 3,5-di-*tert*-butylphenyl substituents were selected to provide excellent solubility. Notably, we were interested in monomeric species, which renders our current approach different from a recently published diazananographene-cobalt(II) porphyrin coordination polymer.[68]

The corresponding pyridine coordination compounds were formed by ligand exchange at room temperature. Solely **RuP-2-RuP** had to be heated to solubilize **2**. **RuP-1** and **RuP-2-RuP** were purified by silica chromatography, a fact which underlines the remarkable strength of the ruthenium-pyridine coordination. Evidence for the complex formation as well as its 3D structure came from NMR, as exemplarily depicted for **RuP-1** in **Figure 2**. When coordinated to **RuP**, the *ortho*-pyridine proton (10) resonances experience a significant up-field shift of 6.6 ppm compared to **1**. It is due to the shielding ring current of **RuP**, which affects those protons that are located close to the center of the macrocycle. A similar up-field shift regarding the *ortho*-pyridine proton resonances is observed for every porphyrin coordination compound; from 8.53 ppm for free pyridine to 2.02 ppm for **RuP** in $C_6D_6$; from 10.67 ppm for **2** in *o*-DCB-$d_4$ to 4.11 ppm for **RuP-2-RuP** in $C_6D_6$. The close proximity is furthermore supported by nuclear Overhauser effect (NOE) experiments, where NOE's between **1** and the metalloporphyrin are measured.

### 2.2. Photophysical Characterization

#### *2.2.1. Steady-State Absorption and Emission of Molecular Nanographenes*

**HBC** was used as a reference for the molecular nanographenes. The absorption spectrum of **1** (**Figure 3a**) strongly resembles that of **HBC**; only minor redshifts and slightly higher extinction coefficients are discernable. This confirms that all of the **1** transitions are of $\pi$–$\pi^*$ nature. In agreement with previous reports,[46] n-$\pi^*$ transitions involving the nitrogen lone pair are expected to appear at higher energies than those that we probed. The most intense absorptions for **1** maximize at 344 and 361 nm. They correspond to $\beta'$- and $\beta$-transitions, respectively, and are assigned to ($S_{n'}$) and ($S_n$) transitions.[10] The p-band at 389 nm stems from ($S_2$) and the $\alpha$-transitions at ≈450 nm are assigned to ($S_1$). Both p- and $\alpha$-electronic transitions are symmetry-forbidden in $D_{6h}$ **HBC**, but gain intensity in $C_{2v}$ **1** as a result of symmetry breaking. This effect is more prominent for the $\alpha$-transitions, which are characterized by rather small extinction coefficients and a complex vibronic progression (Figure 3a, inset). For **2**, all of the aforementioned transitions are shifted to lower energies due to an increase in $\pi$-conjugation. Once again, all transitions are $\pi$-$\pi^*$ in nature. $\beta'$- and $\beta$-transitions with their corresponding maxima at 418 and 442 nm are assigned to ($S_{n'}$) and ($S_n$), respectively. They retain a similar shape to that of **1**, but the molar absorption coefficients are more than three times weaker in **2**. Instead, the p- and $\alpha$-absorptions differ sharply from those of **1**. They are more symmetry-allowed in $D_{2h}$ **2**, as a consequence of the lateral $\pi$-extension. The p-band absorptions of ($S_2$) at 545 and 507 nm correspond to the 0–0* and 0–1* vibronic transitions, respectively. The $\alpha$-band assigned to ($S_1$) appears in the form of a weak shoulder at 567 nm. Important is to note that the energetic difference

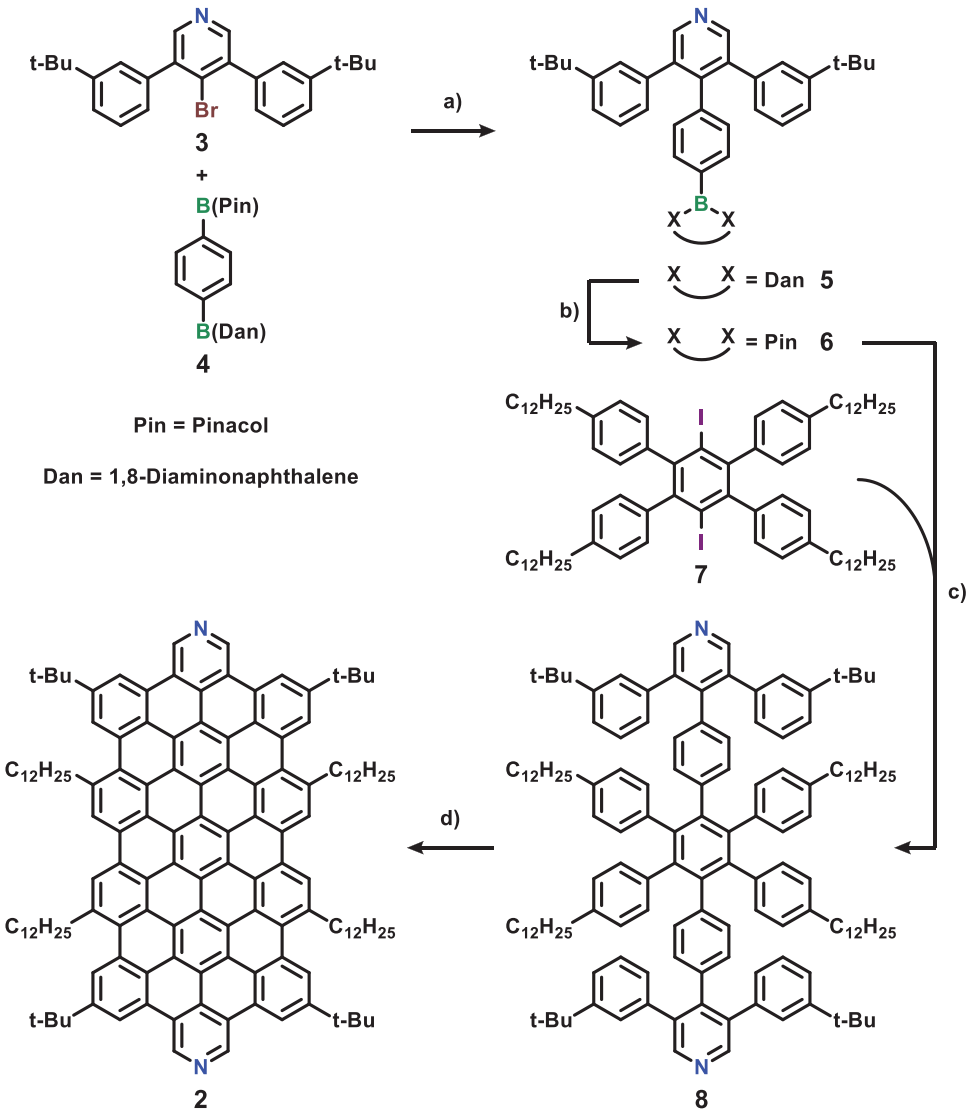


**Scheme 1.** Synthesis of diazananographene **2**. Reagents and conditions: a) $Cs_2CO_3$ (2 equiv.), 5 mol% $Pd(PPh_3)_4$, THF/$H_2O$ (5:1), 3 d, 80 °C, Ar, 82%; b) pinacol (10 equiv.), $H_2SO_4$ (2 M in $H_2O$, 12 equiv.), THF, 2 d, 50 °C, air, 87%; c) $Cs_2CO_3$ (6 equiv.), 40 mol% $Pd(PPh_3)_4$, 1,4-dioxane/$H_2O$ (8:1), 10 d, 100 °C, $N_2$, 73%; d) DDQ (17 equiv.), TfOH (34 equiv.), $CH_2Cl_2$, 3 h, 0 °C to rt, $N_2$, 70%.

between ($S_1$) and ($S_2$) is 3500 $cm^{-1}$ (0.43 eV) for **1** and 700 $cm^{-1}$ (0.09 eV) for **2**. TD-DFT excited state calculations, using a double-hybrid functional (TD-B2PLYP/def2TZVP) to provide a balanced description of the lowest-lying excited states[69] predict, for **2**, an energy difference of 726 $cm^{-1}$ (0.09 eV) between ($S_1$) and ($S_2$). Hereby, the lowest energy transition is much weaker than the next higher one, which is in excellent agreement with the experimental results (**Figure** 4b). For **1**, the ($S_1$)-($S_2$) energy difference is predicted to be 3065 $cm^{-1}$ (0.38 eV, Table S1, Supporting Information). This is also in very good agreement with the experimental data.

At concentrations exceeding $5 \times 10^{-8}$ M, **2** aggregates noticeably in solution resulting in the formation of dimers or higher-order aggregates. In toluene the absorption spectrum of **2** broadens and shifts to lower energies as the concentration is increased (Figure S49, Supporting Information). **1** lacks any of these changes due to its smaller $\pi$-core size in comparison to **2**, which, together with the *tert*-butyl substituents, avoids aggregation in the concentration range employed for our spectroscopic studies.

The fluorescence spectrum of **1** mirror images the $\alpha$-absorptions, much like what is seen for **HBC** (Figure S50, Supporting Information). It is dominated by a vibronic progression including features at 465, 493, and 529 nm, (Figure 3b). This suggests Franck–Condon (FC) vibronic activity for the vibrational frequencies in the 1200 to 1400 $cm^{-1}$ range. The computed FC activities (see the Supporting Information for details) are significant for the three modes at 1281, 1349, and 1380 $cm^{-1}$. The resulting vibronic structure for the ($S_1$) emission matches rather well the observed progression (Figure S42, Supporting Information). The fluorescence of **2** is, like its absorption, red-shifted with respect to **1**. As a matter of fact, for **2** the highest energy fluorescence is

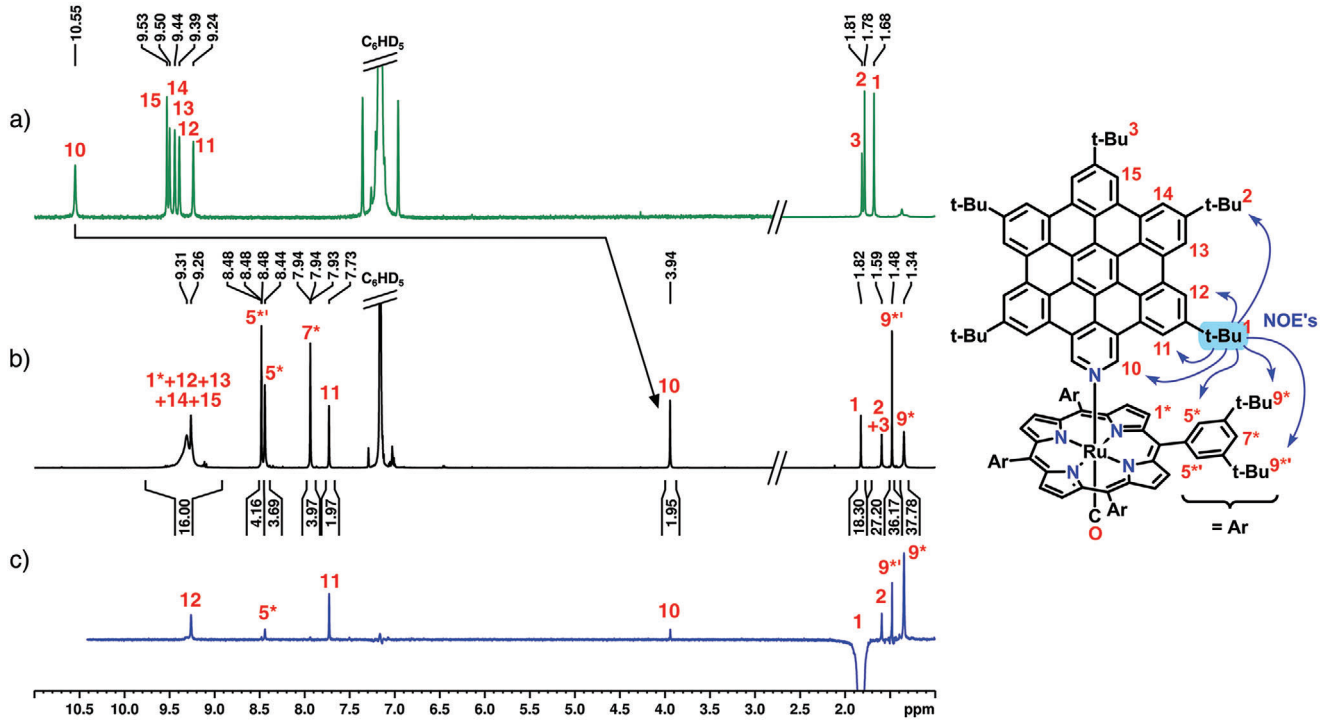


**Figure 2.** a) $^{1}$H NMR of **1** ($C_6D_6$, 400 MHz, rt). b) $^{1}$H NMR of **RuP-1** ($C_6D_6$, 600 MHz, rt). c) NOE of **RuP-1** ($C_6D_6$, 600 MHz, rt) selected for the resonance of proton 1.

recorded at 553 nm, while the most intense fluorescence evolves at 568 nm. Interesting is the fact that the highest-energy fluorescence evolves at higher energies than the lowest-energy absorption (Figure 4b). Moreover, the fluorescence spectrum shape mismatches the absorption spectrum one (Figure S50, Supporting Information). These results point strongly toward a violation of Kasha´s rule for **2** (vide infra). Fluorescence quantum yields in argon-purged toluene are 12% for **1** and 61% for **2**. Both are higher than the 6.7% for **HBC** and indicate that both nitrogen doping and lateral $\pi$-extension boost the emission of molecular nanographenes. In line with this trend are the radiative rate constants, which are $1.2 \times 10^6$ $s^{-1}$ for **HBC**, $5.7 \times 10^6$ $s^{-1}$ for **1**, and $2.2 \times 10^7$ $s^{-1}$ for **2** (**Table 1**). Aggregation of **2** is evident in the fluorescence spectra upon increasing the overall concentration, as also observed in the absorption spectra (Figure S49, Supporting Information). From a broad and unstructured fluorescence, which maximizes at 590 nm, we infer aggregates with an eximeric nature. Phosphorescence for **1** was observed in a Me-THF glass matrix at 80 K (Figure S51, Supporting Information). It is structured and dominated by 565 and 621 nm maxima. In the

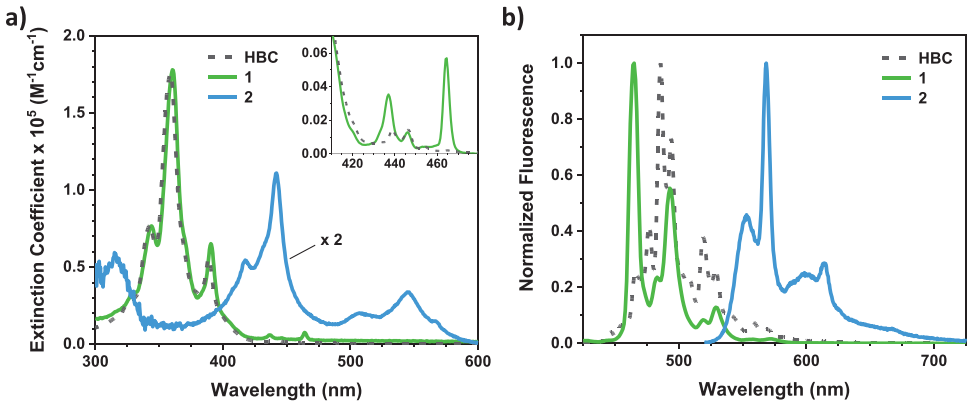


**Figure 3.** a) Absorption spectra of **HBC** (dashed black line), **1** (solid green line), and **2** (solid blue line) in toluene at room temperature. Inset: zoom in on the alpha absorption band of **HBC** and **1**. The absorption of **2** was multiplied by two for clarity reasons. b) Fluorescence spectra of **HBC** upon photo-excitation at 360 nm (dashed black line), **1** upon photo-excitation at 360 nm (solid green line), and **2** upon photo-excitation at 440 nm (solid blue line) in toluene at room temperature. The absorption and fluorescence of **2** were recorded at concentrations of $1 \times 10^{-8}$ and $3 \times 10^{-9}$ M, respectively, to avoid the formation of aggregates.

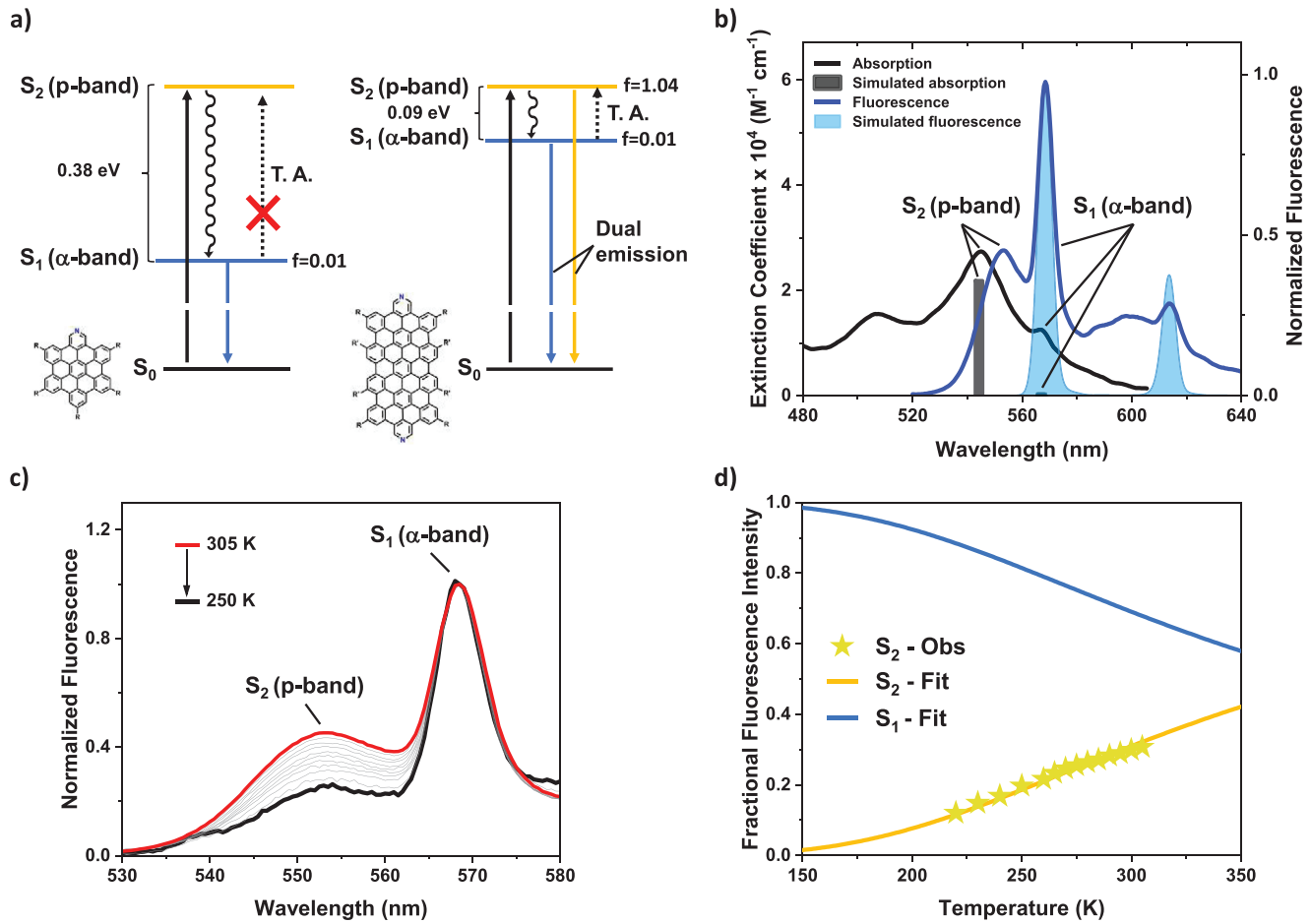


**Figure 4.** a) Schematic illustration of the dual fluorescence by thermal activation (T. A.) taking place only in **2** as a result of the lateral $\pi$-extension. The energy difference between ($S_1$) and ($S_2$) and their corresponding oscillator strength is reported. b) Absorption (black) and fluorescence (blue) of **2** at room temperature and simulated absorption (grey bar) and Franck–Condon vibronic structure (light blue) in the ($S_1$) fluorescence of **2**. Absorption spectra simulated from TD-B2-PLYP/def2TZVP calculations. *Please note that* the vibronic structure is not included. Franck–Condon vibronic structure simulated from CAM-B3LYP/def2SVP and TD-CAM-B3LYP/def2SVP calculations. c) Fluorescence of **2** at different temperatures, that is, from 305 K (red) to 250 K (black). d) Observed fractional fluorescence of the p-transition at different temperatures (yellow), given by the fluorescence intensity of the p-band at 553 nm divided by the sum of the intensity of both the p- and $\alpha$-bands at 553 and 565 nm, respectively. The ocher line is the fit of the fractional fluorescence intensity of the ($S_2$) emission via Equation S1 (Supporting Information). The blue line is the fractional fluorescence intensity associated with the ($S_1$) fluorescence, given simply by one minus the fitted value of fractional fluorescence intensity for the ($S_2$) emission.

case of **2**, aggregation at low temperatures hampered the recording of phosphorescence spectra.

In light of the observed anti-Kasha behavior of **2**, we further investigated its fluorescence to understand its origin. As a matter of fact, the thermal population of the higher lying ($S_2$) from ($S_1$) seems feasible already at room temperature, given the energetic proximity between the p- and $\alpha$-transitions. TDDFT calculations are well in line with this postulate (Figure 4). In addition, the oscillator strength of ($S_2$), which is much higher than that of ($S_1$), prompts radiative processes starting from ($S_2$). In other words, **2** satisfies all those requirements for a thermally-activated dual fluorescence. Considering the complexities of fulfilling such conditions, thermally activated dual fluorescence is quite rare.[70,71] To further support this hypothesis, we simulated the vibronic progression of **2** for the emission from the lowest electronic excited state. The resulting computed fluorescence spectra clearly account for one of the series of sharp peaks, which is symmetric to the $\alpha$-absorption (Figure 4b). FC vibronic activity calculations show that these bands are due to CC stretching modes with computed frequencies of 1321 and 1331 $cm^{-1}$ (Table S2, Supporting Information). This confirms that any other features must originate from higher-lying excited states, namely ($S_2$), that are linked to the p-transition. To prove that thermally-activated

**Table 1.** Fluorescence quantum yields, ($S_1$) lifetimes, and radiative rate constants in inert atmosphere and air-equilibrated toluene.

| | FQY | FQY (Air) | $\tau$ $S_1$ [ns] | $\tau$ $S_1$ (Air) [ns] | $k_r \times 10^6$ [$s^{-1}$][b)] |
|---|---|---|---|---|---|
| **HBC** | 0.07 | 0.04[a)] | 54.7 | 20.3 | 1.2 |
| **1** | 0.12 | 0.09 | 21.7 | 12.2 | 5.7 |
| **2** | 0.61 | 0.38 | 31.3 | 16.5 | 22 |

[a)] Reported from ref. [73]; [b)] Determined as $k_r = FQY \times \tau$ ($S_1$).

fluorescence is taking place, temperature-dependent fluorescence measurements were performed. Lowering the temperature led to a decrease of the ($S_2$) fluorescence (p-band) relative to the ($S_1$) fluorescence ($\alpha$-band), in accordance with the Boltzmann equation (Figure 4c). The relative fluorescence intensity of ($S_1$) versus ($S_2$), namely the fractional fluorescence intensity,[72] nicely matches our theoretical predictions across a large temperature range (Figure 4d, see Supporting Information for details). Important is to notice that for **1** no prominent variations of the fluorescence were observed with temperature, even when cooled down to 80 K (Figure S51, Supporting Information). Recently, thermal equilibrium between a dark ($S_1$) and a bright ($S_2$) was postulated in graphene nanoribbons that bear structural resemblance with **2**.[28] No direct insights into the nature of the dark state were, however, given.[26,27]

### 2.2.2. Time-Resolved Emission of Molecular Nanographenes

Fluorescence lifetimes were determined via time-correlated single photon counting (TCSPC) in argon-purged toluene at room temperature. Large polycyclic aromatic hydrocarbons are generally characterized by long-lived singlet excited states, as a result of the symmetry-forbidden nature of the lowest energy transition. A lifetime of 21.7 ns was, for example, recorded for **1** (Figure S59, Supporting Information). For monomeric **2**, a lifetime of 27.1 ns is noted (Figure S60, Supporting Information). These two lifetimes, together with that of 54.7 ns for **HBC**,[73] follow the general trend given by the oscillator strengths of the respective lowest energy transitions in **HBC**, **1**, and **2**.[74] In reference to the relationship between the Einstein coefficients of absorption and fluorescence, a smaller molar absorption coefficient of the lowest-lying transition leads to smaller radiative rate constants, and, in turn, to longer fluorescence lifetimes. Owing to the long-lived nature of the singlet excited state, it is quenched by dioxygen via a diffusion-controlled mechanism.[74] This is supported by shorter singlet excited state lifetimes and lower fluorescence quantum yields when going from argon-purged to air-equilibrated solutions (Figures S59 and S60, Supporting Information); 12.2 ns and 8.6% for **1** as well as 15.1 ns and 38% for **2** (Table 1). To better investigate the emission of aggregated **2**, time-resolved fluorescence spectra were also recorded in argon-purged toluene at concentrations where monomers and aggregates coexist (Figure S61, Supporting Information). Fitting the raw data with a parallel two-species model allowed the deconvolution of the fluorescence spectra of the aggregate and of the monomers. Besides the fluorescence of monomeric **2**, a broad and red-shifted fluorescence at ≈580 nm with a lifetime of 5.3 ns is associated to **2** aggregates.

### 2.2.3. Steady-State Characterization Upon RuP Coordination

**RuP** was used as a reference. In the absorption spectrum of **RuP-1** (**Figure 5**), all transitions are centered on either the metalloporphyrin or **1**, while no evidence for a charge-transfer band is discernable. Those centered on the metalloporphyrin are, however, weaker in **RuP-1** than in **RuP**, albeit their energies are not affected at all. Instead, all absorptions associated with **1** are red-shifted and intensified in **RuP-1**, as a result of coordination. For example, the $\beta$-transition shifts from 360 to 364 nm with an increase of its molar extinction coefficient from $1.8 \times 10^5$ to $2.3 \times 10^5$ $M^{-1}\,cm^{-1}$. Importantly, the lowest energy transition is the porphyrin-centered Q-band absorption at 565 nm. **RuP-2-RuP** is just like **RuP-1**, with the lowest energy transition corresponding to the Q-band absorption of the metalloporphyrin, which is, in turn, nearly isoenergetic to the $\alpha$-band of **2**. TDDFT calculations were employed to gather insights into the electronic structure of **RuP-1** and **RuP-2-RuP**. For both of them, the calculated electronic transitions match well the experimental absorption spectra (Figure S44, Supporting Information). Most importantly, analyses of the TDDFT data support the notion that the low energy transitions in both **RuP-1** and **RuP-2-RuP** are metalloporphyrin-centered, while transitions with charge-transfer nature are not discernable (Figures S45 and S46, Supporting Information).

By virtue of the heavy atom effect,[75] phosphorescence rather than fluorescence was detected for **RuP**.[76,77] It shows a maximum at 735 nm with a shoulder at ≈820 nm (Figure S52, Supporting Information). Similarly, **RuP-1** is dominated by the **RuP** phosphorescence, regardless of selective photo-excitation of **RuP** or **1** at either 415 or 362 nm, respectively (Figure 5b). The latter implies an energy transfer from **1** to **RuP**, as observed in covalently linked **HBC**-porphyrin conjugates.[49] Independent confirmation comes from the fact that the absorption spectrum of **RuP-1** matches the excitation spectrum when monitoring the phosphorescence at 750 nm (Figure S53, Supporting Information). **RuP-2-RuP** behaves similarly. Selective photo-excitation of **RuP** or **2** at either 420 or 442 nm, respectively, leads to **RuP** phosphorescence (Figure 5d). In contrast, the phosphorescence intensity in **RuP-2-RuP** is substantially weaker than either in **RuP** or in **RuP-1** (Figure S52, Supporting Information). Implicit is an additional deactivation pathway that impacts the triplet excited state of the metalloporphyrin in **RuP-2-RuP** and that is absent in **RuP** and **RuP-1**. The corresponding phosphorescence quantum yields are less than 0.01% for all of them, which were too low to draw any meaningful comparisons. Photodegradation, as already reported to occur for **RuP**,[78–82] is also operative for **RuP-1** and **RuP-2-RuP** (see details in the SI). But, to a much lesser extent, which stresses the higher photostability of these latest (Figure S58, Supporting Information).

### 2.2.4. Excited State Dynamics of Molecular Nanographenes

Transient absorption spectroscopy (TAS) with femto-to-nanosecond resolution was further employed to investigate the excited state decay in argon-purged toluene at room temperature. Upon photo-excitation at 387 nm, two excited state absorptions (ESA) are discernable in the fs-TAS of **1** at 460 and 550 nm (Figure S63, Supporting Information). Global fitting of the data revealed two exponential processes with lifetimes of 150 ps and longer than 10 ns. Therefore, a two-species sequential model was applied, by which we obtained two evolution-associated differential spectra (EAS) that are quite similar to each other. The first species should be associated to ($S_2$), which is populated by the 387 nm photo-excitation (p-band at 389 nm), and, which converts in 150 ps to ($S_1$) as the second species. Similar lifetimes were previously reported for other molecular nanographene and

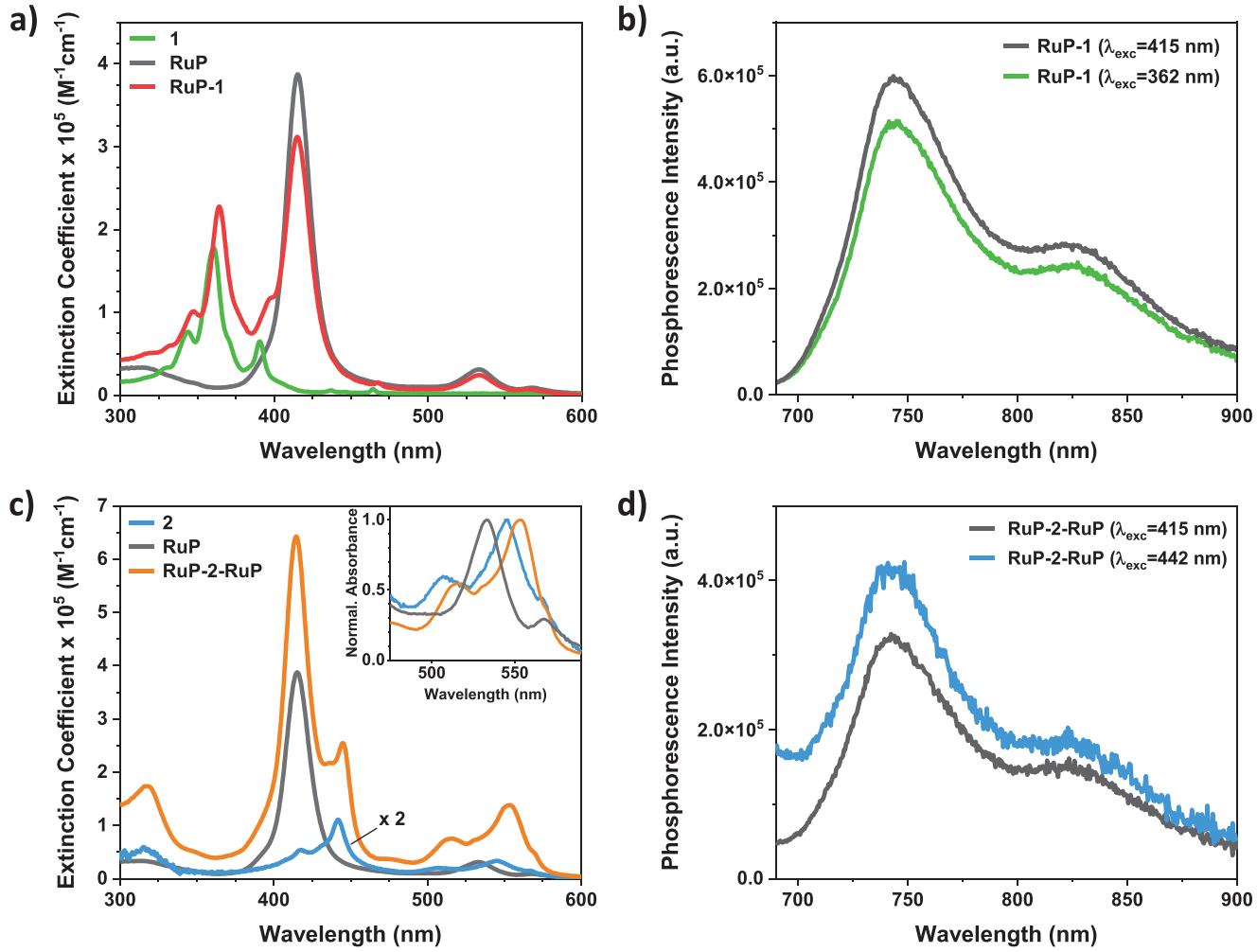


**Figure 5.** a) Absorption spectra of **1** (green), **RuP** (black), and **RuP-1** (red) in toluene at ambient conditions. b) Phosphorescence spectra of **RuP-1** in argon-purged toluene. The porphyrin-centered phosphorescence is observed both when photo-exciting selectively either **RuP** at 415 nm (black) or **1** at 362 nm (green), proving the occurrence of an energy transfer from **1** to **RuP**. c) Absorption spectra of **2** (light blue), **RuP** (black), and **RuP-2-RuP** (orange) in toluene at ambient conditions. Inset: magnification of the lowest energy absorption bands, normalized with respect to their relative maxima. The **RuP** $Q_{00}$ band appears to be the lowest energy transition, being, however, really close in energy with the $\alpha$-band of 2. b) Phosphorescence spectra of **RuP-2-RuP** in argon-purged toluene. The porphyrin-centered phosphorescence is observed when photo-exciting selectively **RuP** at 415 nm (black) or 2 at 442 nm in light blue, proving the energy transfer from **2** to **RuP**. All the emission spectra were corrected for the absorbance at the excitation wavelength.

graphene nanoribbons.[73,83,84] They are, however, too long-lived to stem from vibrational relaxation in a rigid scaffold such as **1**. ns-TAS allowed to follow the complete decay of the excited state (**Figure 6**). Upon photo-excitation at 400 nm, other than the two ESAs at 460 and 550 nm, ground state bleachings (GSBs) at 365, 390, and 465 nm are discernable at early time delays. With increasing time, the feature linked to the singlet decreases in intensity, while a new species is formed. The latter is characterized by an ESA at 500 nm. It is attributed to the triplet excited state ($T_1$), which fully decays to the ground state in tens of microseconds. Global fitting is achieved with a biexponential sequential model, leading to lifetimes of 20.9 ns for ($S_1$) and 39.9 µs for ($T_1$). The deconvoluted EAS and the excited state dynamics via both fs-TAS and ns-TAS strongly resemble those observed for **HBC**.[73]

Upon photo-excitation at 420 nm, intense GSBs are noted at 444, 520, and 560 nm (Figure S64, Supporting Information) in the fs-TAS of **2**. ESAs evolve at 485, 600, 800, and 900 nm. It is only the latter, which fades with increasing time delays, while the remaining GSBs and ESAs are subject to subtle intensity decreases. It should be pointed out that the poor solubility of **2** resulted in spectra with a low signal-to-noise ratio, which prevented us from gathering any additional kinetic insight into the thermal equilibration between ($S_2$) and ($S_1$). Global fitting of the data revealed three exponential processes. Therefore, a three-species sequential target model was applied. The first species is an upper singlet excited ($S_{n'}$) state, populated upon 420 nm photo-excitation into the $\beta$'-band at 418 nm. Vibrational relaxation and internal conversion take place within 1 ps to afford ($S_1$). The remaining two species relate to ($S_1$) of either monomeric **2** or

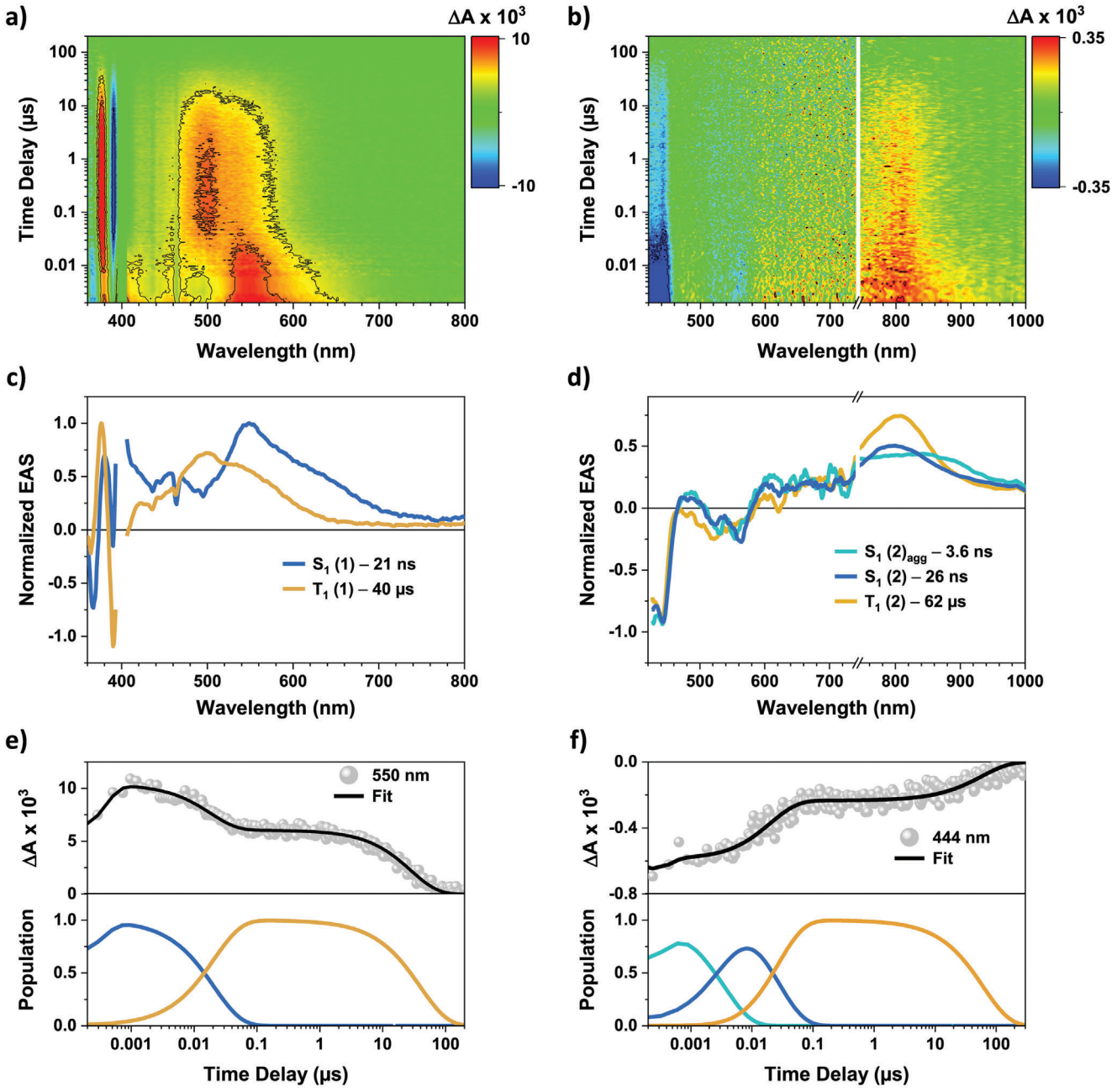


**Figure 6.** Nanosecond transient absorption raw data and corresponding fits for **1** (a, c, and e) and **2** (b, d, and f) in argon-purged toluene at room temperature upon photo-excitation at 400 and 420 nm, respectively. a) Heat map of ns-TAS raw data of **1** obtained from pump-probe experiments with time delays up to 200 μs. b) Heat map of ns-TAS raw data of **2** obtained from pump-probe experiments with time delays up to 200 μs. c) Normalized evolution-associated spectra (EAS), resulting from the global fit of the raw data with a sequential two-species model. The first species in blue is ($S_1$) of **1** and the second species in ochre is ($T_1$) of **1**. d) Normalized evolution-associated spectra (EAS), resulting from the global fit of the raw data with a sequential three-species model. The first species in cyan is ($S_1$) of aggregated **2**, the second species in blue is ($S_1$) of monomeric **2**, and the third species in ochre is ($T_1$) of monomeric **2**. e) Single wavelength kinetics of **1** (top) at 550 nm (grey dots) with its relative fit (black line), and populations dynamic (bottom) of the respective species with colors correlating with the species-associated spectra (SAS) shown in c). f) Single wavelength kinetic of **2** (top) at 444 nm (grey circles) with its respective fit (black line), and population dynamics (bottom) of the respective species with colors correlating with the species-associated spectra (SAS) shown in d).

aggregated **2**. Both of them decay on the nanosecond timescale. The shorter-lived one is linked to an aggregated form of **2**, as the broad GSB between 430 and 460 nm resembles the broad absorption spectrum observed upon aggregation (Figure S49, Supporting Information). The other one relates to monomeric **2**, given the sharper GSB at 444 nm. To follow their complete decays, we employed ns-TAS under 420 nm photo-excitation (Figure 6). On the sub-microsecond timescale, the intensity of the differential spectra is subject to a major decrease. Nevertheless, it takes several hundreds of microseconds to fully decay to the ground state. Global fitting of the data revealed three exponential processes, with lifetimes of 3.6 ns, 26.3 ns, and 61.6 µs. A rather poor signal-to-noise ratio hampered the use of a target model. In accordance with fs-TAS and TCSPC measurements, the first two are assigned to ($S_1$) of aggregated **2** and monomeric **2**, respectively. ($S_1$) of aggregated **2** decays directly to the ground state, while ($S_1$) of monomeric **2** feeds ($T_1$), which has a lifetime of 61.6 µs. Comparing the EAS of ($S_1$) and ($T_1$) the latter lacks the 485 nm ESA, while the 800 nm ESA appears more intense.

### *2.2.5. Excited State Dynamics of Coordination Compounds*

Energy transfer as observed for **RuP-1** and **RuP-2-RuP** in the steady-state emission experiments was studied using fs- and ns-TAS. fs-TAS of **RuP** upon photo-excitation at 420 nm affords characteristic ESAs for ($T_1$) of metalloporphyrins, which is persistent during the fs-TAS time-window (Figure S65, Supporting Information). Its differential spectrum is characterized by a strong 485 nm ESA, followed by three less intense ESAs appearing at 555, 585, and 860 nm. Weak GSBs are observed at 430 and 535 nm. Indeed, by virtue of the heavy atom effect, the intersystem crossing from ($S_1$)-to-($T_1$) is faster than our instrumental resolution. As such ($S_1$) of **RuP** was unobservable to us. In the ns-TAS, we followed the complete decay of ($T_1$) (Figure S66, Supporting Information). Global fitting with a mono-exponential decay function afforded a 28.9 µs ($T_1$) lifetime.

For **RuP-1**, a 387 nm pump was utilized in fs-TAS to ensure the prevalent photo-excitation of **1** (**Figure 7**). Spectral fingerprints for ($S_1$) of **1**, that is, ESAs at 455 and 550 nm, are appreciated at early time delays. Most importantly, their decay is linked to the rise of a series of novel features. For example, a newly developing ESA at 484 nm matches perfectly the fingerprint of ($T_1$) in **RuP** (Figure S65, Supporting Information). Global fitting of the data revealed a mono-exponential process with a lifetime of 7.0 ps next to a long-lived component. A two-state sequential model (**Figure 8**) was employed, which considers that **1** and **RuP** are populated upon photo-excitation in a 3:1 ratio, based on their molar absorption coefficients at 387 nm. The first species is ($S_1$) of **1**, while the second species corresponds to ($T_1$) of **RuP**. As a consequence, the picosecond lifetime is associated with an inter-component energy transfer process. The decrease of the ($S_1$) lifetime from 21.7 ns in **1** to 7.0 ps in **RuP-1** is linked to a rate constant of $1.4 \times 10^{11}$ $s^{-1}$ for the underlying energy transfer that is unit efficient. Rather than a spin-forbidden ($S_1$)-to-($T_1$) energy transfer, we postulate a spin-allowed ($S_1$)-to-($S_1$) energy transfer followed by a rapid ($S_1$)-to-($T_1$) intersystem crossing. The latter process is spectroscopically invisible as ($S_1$) of **RuP** decays faster than it is populated.

In the case of **RuP-2-RuP**, pumping at 550 nm ensured the almost selective photo-excitation of **2**. In fs-TAS, already visual inspection of the kinetic trace at 444 nm revealed the occurrence of two processes, in contrast to **RuP-1** (Figure 7e,f). For example, the transient absorption spectra at early time delays are a good match of the differential spectrum of ($S_1$) of monomeric **2**. In particular, GSBs at 445 and 515 nm as well as ESAs at 800 and 900 nm are noted (Figure S67, Supporting Information). With increasing time delays, these transients disappear with the concomitant rise of the characteristic ($T_1$) of **RuP**, namely ESAs at 475 and 850 nm next to a GSB at 850 nm, as observed for **RuP-1**. However, in stark contrast to the latter, ($T_1$) of **RuP** decays almost completely on the fs-TAS timescale. This goes hand-in-hand with the evolution of GSBs at 445 and 515 nm and an intense ESA at 800 nm. All the aforementioned correspond to ($T_1$) of **2**. Global fitting of the data revealed the presence of three exponential processes next to an infinite component. Accordingly, a four-species target model was applied (Figure 8). The first two species are the vibrationally hot and relaxed singlet excited state of **2** — ($^*S_1$) (**2**) and ($S_1$) (**2**) — with 1 and 22 ps lifetimes, respectively. For **RuP-2-RuP**, the ($S_1$) lifetime of **2** is three orders of magnitude shorter than for uncoordinated **2**. This corroborates a quantitative energy transfer to yield ($T_1$) of **RuP**, with an underlying rate constant of $4.5 \times 10^{10}$ $s^{-1}$.

We postulate also here a spin-allowed ($S_1$)-to-($S_1$) energy transfer followed by a rapid ($S_1$)-to-($T_1$) intersystem crossing.[74] The ($T_1$) lifetime of **RuP** is 2.7 ns and ($T_1$) of **2** evolves as a product. In other words, a "ping-pong" energy transfer from **2** to **RuP** and back to **2** is evidenced. The rate constant of a quantitative back energy transfer is $3.5 \times 10^8$ $s^{-1}$. In fs-TAS upon prevalent photo-excitation of **RuP** at 420 nm the exact same deactivation scheme was concluded (Figure S68, Supporting Information). Only the relative population of the respective species differed. ns-TAS was employed to follow the deactivation of the final product of the energy transfer cascade. Upon selective photo-excitation of **RuP** in **RuP-2-RuP** at 420 nm, the transients associated with ($T_1$) of **RuP** are observed to feed the population of ($T_1$) in **2** (Figure S69, Supporting Information). Global fitting revealed three exponential processes and target analysis based on a three-species model was applied. The first two species are those involved in the spin-allowed ($T_1$)-to-($T_1$) energy transfer, which takes 2.9 ns. Energy transfer is eventually followed by the ($T_1$) decay to the ground state with a lifetime of 27.8 µs. The latter is less than half of that derived for monomeric **2**, most likely the heavy atom effect causes the underlying acceleration. In the presence of dioxygen, ($T_1$) of **2** is strongly quenched. This confirms the overall ($T_1$) nature and excludes any charge transfer or charge separation channels (Figures S71 and S72, Supporting Information). The third species that was used for the fitting is attributed to ($S_1$) of some monomeric **2** in solution,[85] resulting from photodegradation (See Supporting Information for details).

We attribute the modulation of excited state deactivation when going from **RuP-1** to **RuP-2-RuP** to an increase of $\pi$-conjugation in the latter case, which affected the energy of ($S_1$) and ($T_1$) to a similar extent (Figure 8a; Table S3, Supporting Information). As a matter of fact, the energy decreases of ($S_1$) when comparing **1** and **2** is very close to that seen for ($T_1$). Overall, $\Delta E$ ($S_1$-$T_1$) remains unchanged, which is in agreement with the similar nature of the

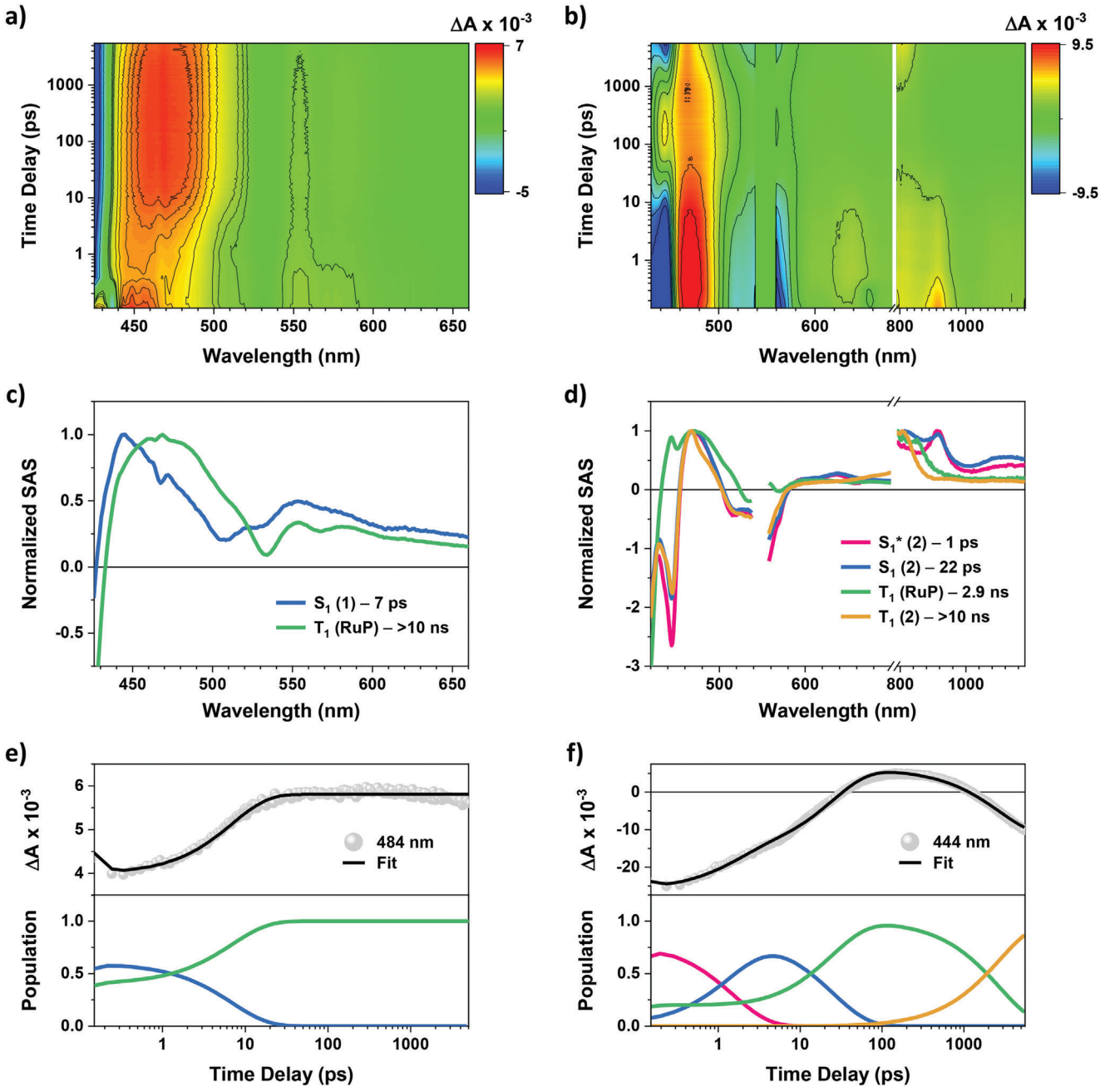


**Figure 7.** Femtosecond transient absorption raw data and corresponding fits for **RuP-1** (a, c, and e) and **RuP-2-RuP** (b, d, and f) in argon-purged toluene at room temperature upon photo-excitation at 387 and 550 nm, respectively. a) Heat map of fs-TAS raw data of **RuP-1** obtained from pump-probe experiments with time delays up to 5500 ps. b) Heat map of fs-TAS raw data of **RuP-2-RuP** obtained from pump-probe experiments with time delays up to 5500 ps. c) Normalized species associated spectra (SAS) of **RuP-1** resulting from the global fit of the raw data with a target two-species model. The first species in blue is ($S_1$) of **1** ($\tau$ = 7 ps), while the second one in green is ($T_1$) of **RuP** ($\tau$ = >10 ns). d) Normalized species-associated spectra (SAS) resulting from the global fit of the raw data with a target four-species model. The first species in violet is ($S_1$*) centered on **2** ($\tau$ = 1 ps); the second species in blue is ($S_1$) of **2** ($\tau$ = 22 ps); the third species in green is ($T_1$) of **RuP** ($\tau$ = 2.9 ns); the last state in ochre is ($T_1$) of 2 ($\tau$ = >10 ns). e) Single wavelength kinetics of **RuP-1** (top) at 484 nm (grey dots) with its relative fit (black line), and relative populations dynamics (bottom) of the respective species with colors correlating with the species-associated spectra (SAS) shown in (c). f) Single wavelength kinetic of **RuP-2-RuP** (top) at 444 nm (grey circles) with its respective fit (black line) and relative population dynamics (bottom) of the respective species with colors correlating with the species-associated spectra (SAS) shown in (d).

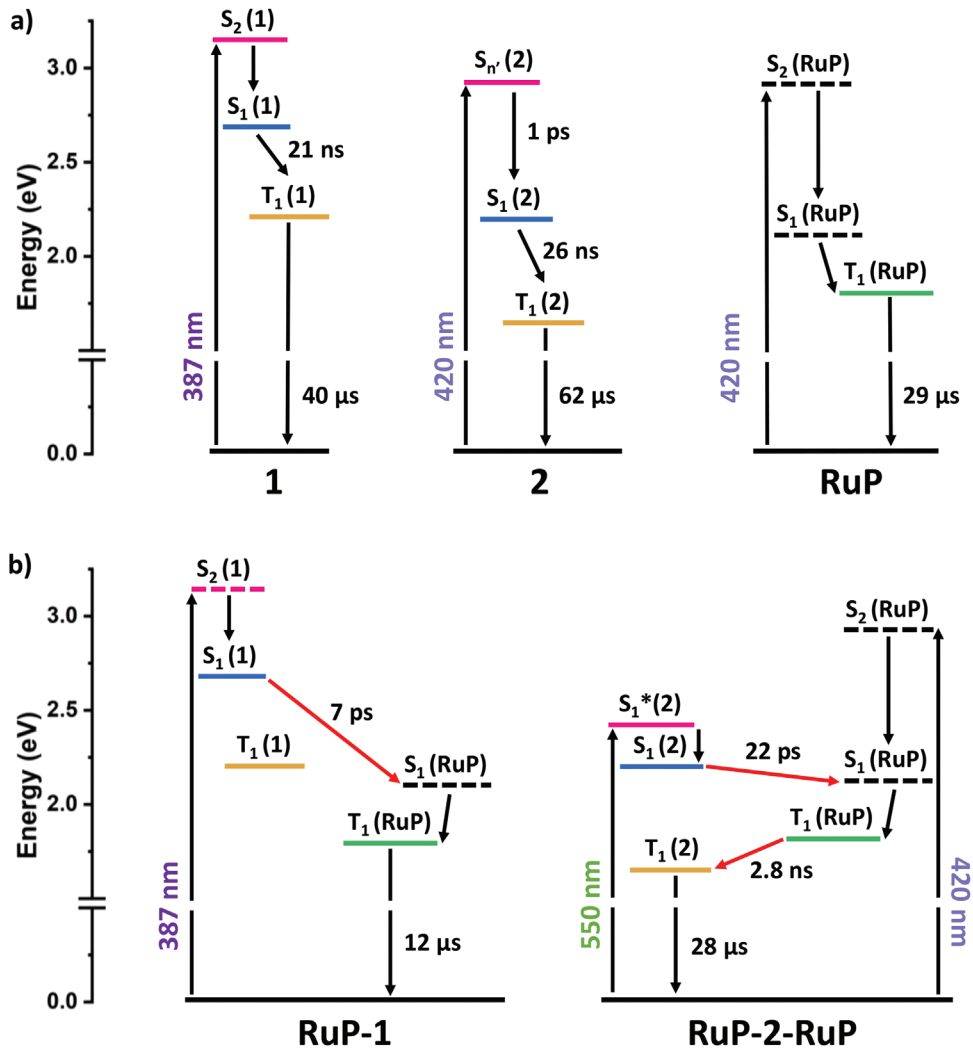


**Figure 8.** a) Proposed deactivation scheme and lifetimes for **1** upon photo-excitation at 387 nm, on the left, for **2**, in the center, and **RuP**, on the right, upon photo-excitation at 420 nm. b) Proposed deactivation scheme and lifetimes for **RuP-1** upon photo-excitation at 387 nm, on the left, and for **RuP-2-RuP** upon photo-excitation at 550 and 420 nm, on the right. The dashed states for $S_n$ (**1**), $S_2$ (**RuP**), and $S_1$ (**RuP**) point out that they cannot be observed being either their lifetime shorter than our instrumental resolution, for the first two, or because it is spectroscopically invisible, for the last one, being its deactivation faster than its population. The red arrows indicate the deactivation via energy transfer. The number on each arrow indicates the lifetime of the starting state as determined in transient absorption spectroscopy experiments. The energies were obtained from the absorption, fluorescence, and phosphorescence spectra and are supported by TDDFT calculations as well at B3LYP-D3BJ/ def2-TZVP level of theory (Table S3, Supporting Information).

lowest excited state for both **1** and **2**, as shown by calculations (Figure S40, Supporting Information).

For both **RuP-1** and **RuP-2-RuP**, **1** and **2** are perpendicular to the plane of **RuP**, as observed via both NMR analysis and quantum chemical calculations. Furthermore, the latter supports the fact that the transition dipole moments associated with the excited states involved in the energy transfer are also in a perpendicular orientation to each other (Figure 2; Figures S14, S47, and S48, Supporting Information). Therefore, a coulombic mechanism based on dipole interactions should be excluded.[74] In light of this, we postulate an exchange mechanism to be operative in the transfer of energy. Forward energy transfer rate constant ($k_{ET}$) in **RuP-1** ($1.4 \times 10^{11}$ $s^{-1}$) and **RuP-2-RuP** ($4.5 \times 10^{10}$ $s^{-1}$) differ by a factor of three. A reasonable rationale is based on the differences related to the Franck-Condon factors associated with the two processes. In the case of **RuP-2-RuP**, the FC factor is small due to the nearly isoenergetic ($S_1$) for **2** and of **RuP**. In other words, the overlap between **2** emissions and **RuP** absorption is small. On the contrary, the overlap is significantly larger for **RuP-1**, that is, between **1** emission and **RuP** absorption. The ($T_1$)-to-($T_1$) energy transfer rate constant ($3.5 \times 10^8$ $s^{-1}$) in **RuP-2-RuP**, which is based on an exchange mechanism, is two orders of magnitude smaller than the ones involving the singlet excited states.

### 2.3. Electrochemical Characterization

Electrochemical characterization was performed by both cyclic voltammetry and differential pulse voltammetry (DPV) in dichloromethane (Figures S73–S78, Supporting Information).

**Table 2.** Electrochemical redox potentials (V vs Fc/Fc+) for **1**, **RuP**, **RuP-1**, and **RuP-2-RuP**. The values were determined via DPV in $CH_2Cl_2$ with 0.1 M $TBAPF_6$.

| | $E_{red3}$ [V] | $E_{red2}$ [V] | $E_{red1}$ [V] | $E_{ox1}$ [V] | $E_{ox2}$ [V] | $E_{ox3}$ [V] |
|---|---|---|---|---|---|---|
| **1**[a)] | | | −2.17 | +0.78 | +1.0 | +1.13 |
| **RuP** | | −2.23 | −2.07 | +0.33 | +0.95 | |
| **RuP-1** | | −2.29 | −2.07 | +0.33 | +0.95 | |
| **RuP-2-RuP** | −2.18 | −1.99 | −1.82 | +0.35 | +0.61 | +0.92 |

[a)] Reported from ref. [64].

The results are summarized in **Table 2**. Overall, they are helpful in rationalizing the lack of any charge separation upon photoexcitation. **1** was already studied by some of us[64] and we concluded three oxidations at +0.78, +1.0, and +1.13 V versus $Fc/Fc^+$ next to one reduction at −2.17 V versus $Fc/Fc^+$. The low solubility of **2** precluded its electrochemical characterization when uncoordinated. **RuP** showed two reversible oxidations at +0.31 and +0.89 versus $Fc/Fc^+$, in agreement with previous reports. The reductions are irreversible and are better studied via DPV, appearing at −2.07 and −2.23 V versus $Fc/Fc^+$. **RuP-1** shows similarities to **RuP**, with the first oxidation and the first reduction both centered on the metalloporphyrin. The reductions are, nevertheless, quasi-reversible in this case. Notable, in DPV the second oxidation at +0.95 versus $Fc/Fc^+$ is two times stronger than the first one, suggesting an overlap with the oxidation of **1**. **RuP-2-RuP** differs from **RuP** and **RuP-1**. For example, the first reduction at −1.82 V versus $Fc/Fc^+$ is attributed to **2**. This is based on the comparison of its DPVs with those of **RuP** (Figures S76 and S78, Supporting Information). The second oxidation at +0.61 V versus $Fc/Fc^+$ is also centered on **2**. We conclude that the two metalloporphyrins are electronically isolated from each other. Indeed, all the redox processes centered on the metalloporphyrins are comparable to the reference, and no splitting is observed. Based on these results, charge separation is thermodynamically allowed when considering higher lying ($S_1$) of either **1** or **2**, but not from the lower lying ($T_1$) of either **RuP** or **2**. However, ultrafast energy transfer to afford the lower lying ($T_1$) rules out any charge separation upon photo-excitation, as also observed for other porphyrin-nanographene derivatives.[9]

## 3. Conclusion

To conclude, the presence of a nitrogen atom in the peripheric position of molecular nanographene opens the door to coordinate, for example, metalloporphyrins and, thereby, increases the potential applicability of such molecular architectures. It was also shown to boost the fluorescence quantum yields of molecular nanographene via the increase of radiative rate constant, due to symmetry reduction, but unaltering at the same time the energy of excited states. The lateral $\pi$-extension from **1** to **2** led to a modulation of the excited state energies that resulted in several interesting phenomena. First, the fluorescence quantum yield is as high as 61% for **2**. Second, a thermally-activated dual fluorescence, a process of which not many examples are reported in the literature, was corroborated. In fact, **2** is, to the best of our knowledge, the largest-sized molecule showing this behavior. Third, $\pi$-extension was useful to tune the excited state deactivation of **RuP-1** and **RuP-2-RuP**. A ping-pong energy transfer, meaning from **2** to **RuP** and back to **2**, was observed in the case of **RuP-2-RuP**, in contrast to the simpler energy transfer from **1** to **RuP**, which was recorded for **RuP-1**. Modulation of the excited state deactivation was attributed to the mere increase of $\pi$-conjugation when comparing **2** and **1**, which results in an energy decrease of both ($S_1$) and ($T_1$).

The results reported herein demonstrate that molecular nanographenes are attractive components for solar energy conversion schemes, where inter-component energy transfer can be modulated. Furthermore, our studies start to shed light on the relationship between the structure and photophysical properties of molecular nanographenes, which is essential for their use in practical applications; and prove the great potential of molecular nanographene as models for an in-depth understanding of graphene nanoribbons and quantum dots. Studies with molecular nanographenes of different sizes are currently ongoing in our laboratories.

## 4. Experimental Section

*Photophysical Characterization*: Steady-state absorption experiments of solutions were performed using a Shimadzu UV-1900i UV–vis spectrophotometer double beam spectrometer (190–1100 nm). All spectra were acquired at room temperature using 10 × 10 mm or 100 × 10 mm quartz glass cuvettes. Steady-state emission spectra were recorded on an FS5 spectrofluorometer from Edinburgh Instruments. The data were recorded by using standard 10 × 10 mm quartz cuvettes within optical densities ranging from 0 to 0.1. Fluorescence quantum yields were determined by using 9-phenyl anthracene in cyclohexane for **1** and a perilene diimide in toluene for **2**. To avoid aggregation of the latter, the measurements were performed at concentrations lower than $10^{-8}$ M, employing 100 × 10 mm quartz glass cuvettes for determining the absorbance and 10 × 10 mm quartz glass cuvettes for recording the emission. Emission lifetimes and time-resolved emission spectroscopy (TRES) were measured using a Fluorolog 3 time-correlated photon counting (TCSPC) instrument from Horiba Jovin Yvon, a SuperK Fianium FIU6PP supercontinuum laser from NKT Photonics as the excitation source, and an R3809U-50 MCP photomultiplier from Hammamatsu, or with an Edinburgh FS5 spectrofluorimeter equipped with a VisUV picosecond laser system from PicoQuant (pulse duration <85 ps). Femtosecond transient absorption (fsTA) was conducted using an Astrella-F-1K amplified Ti:sapphire femtosecond laser system from Coherent, operating at a repetition rate 1 kHz, 5.5 W power (5 mJ pulse energy), pulse duration of 80 fs, with TA pump/probe Helios detection system from Ultrafast Systems. White light was generated focusing a fraction of the fundamental 800 nm output onto a 2 mm $CaF_2$ mounted on a translating crystal holder. A 1.2 mJ fraction of the fundamental is used for pump beam generation by a TOPAS Prime from Light Conversion with standard NIRUVIS extension. An optical delay line allowed for time delays up to 7.2 ns. A depolarizer was placed in the pump beam to avoid rotational dynamics. Bandpass filters with ±5 or ±10 nm were used to ensure low spectral width and to exclude 800 nm photons. Additionally, some (fsTA) experiments were conducted employing an amplified Ti:sapphire CPA-2101 laser system from Clark:MXR Inc. as the excitation source. The generated laser pulses were characterized by an initial wavelength of 775 nm, a pulse width of 150 fs, and a frequency of 1050 Hz. The detection of the data was realized using a HELIOS "transient absorption pump-probe system" (TAPPS) detection unit from ultrafast systems. The excitation wavelengths, with energies of roughly 400 nJ, were generated by a noncolinear optical parametric amplifier (NOPA, Clark:MXR Inc.), whereas the white light (probe pulse) was generated by a sapphire crystal. The experiments were carried out using fused quartz glass cuvettes with a width of 2 mm. All of the samples were deoxygenated for ≈15 min

using argon gas and measured at an absorbance of roughly 0.2 at the respective excitation wavelength. For data recording, the HELIOS system from Newport/Ultrafast systems was utilized. Nanosecond transient absorption (nsTA) experiments were recorded with the EOS TAPPS detection unit from Ultrafast systems using two independent pulsed laser sources. While the pump pulse was also generated by an amplified Ti:sapphire CPA-2101 laser system from Clark:MXR Inc., the probe pulse was generated by a pulsed supercontinuum laser (output 350–2200 nm, repetition rate of 2100 Hz, and 1 ns pulse width). The electronic setup allows for time delays of up to 400 µs between the pump and probe pulse. The excitation wavelengths were generated by a noncolinear optical parametric amplifier (NOPA, Clark:MXR Inc.). For the fsTA and nsTA measurements, global as well as target analysis and fitting of the transient data was carried out utilizing the open-source software GloTarAn, which is a free, Java-based graphical user interface to the R-package TIMP.[86–88] The instrument response function (IRF) and dispersion (chirp of the white light pulse) were modeled and taken into account during the fitting procedure. The nsTA data sets were corrected for scattered light as well.

*Electrochemical Characterization*: Cyclic voltammetry and differential pulse voltammetry were performed with a three-electrode setup on AutoLab PGStat302N instrument. The measurements were carried out in dichloromethane using 0.1 M tetrabutylammoniumhexafluorophosphate ($TBA(PF_6)$ as a supporting electrolyte and compound concentration of $\approx 10^{-4}$ M. A platinum rod was used as a working electrode, a platinum wire served as a counter electrode, and a silver wire as a quasi-reference electrode. Ferrocene (Fc) was used as the internal standard and all the potentials were noted relative to the $Fc/Fc^+$ couple. The data were recorded with NOVA 2.0 software.

## Supporting Information

Supporting Information is available from the Wiley Online Library or from the author.

## Acknowledgements

The authors gratefully acknowledge the funding by the Deutsche Forschunggemeinschaft (DFG), project number 182849149-SFB953. FN acknowledges the European Union—Next Generation EU under the Italian National Recovery and Resilience Plan (PNRR M4C2, Investimento 1.4—Avviso n. 3138 del 16/12/2021—CN00000013 National Centre for HPC, Big Data and Quantum Computing (HPC)— CUP J33C22001170001).

Open access funding enabled and organized by Projekt DEAL.

## Conflict of Interest

The authors declare no conflict of interest.

## Data Availability Statement

Research data are not shared.

## Keywords

anti-Kasha emission, coordination complexes, energy transfer, metalloporphyrin, molecular nanographenes

Received: April 5, 2024
Revised: May 21, 2024
Published online: June 11, 2024

[1] X.-Y. Wang, A. Narita, K. Müllen, *Nat. Rev. Chem.* **2017**, *2*, 0100.
[2] Y. Gu, Z. Qiu, K. Müllen, *J. Am. Chem. Soc.* **2022**, *144*, 11499.
[3] J. Wu, W. Pisula, K. Müllen, *Chem. Rev.* **2007**, *107*, 718.
[4] M. Y. Han, B. Özyilmaz, Y. Zhang, P. Kim, *Phys. Rev. Lett.* **2007**, *98*, 206805.
[5] Y.-W. Son, M. L. Cohen, S. G. Louie, *Phys. Rev. Lett.* **2006**, *97*, 216803.
[6] Z. Liu, S. Fu, X. Liu, A. Narita, P. Samorì, M. Bonn, H. I. Wang, Z. Liu, P. Samorì, S. Fu, *Adv. Sci.* **2022**, *9*, 2106055.
[7] F. G. T. Schwierz, *Nat. Nanotechnol.* **2010**, *5*, 487.
[8] A. Narita, X.-Y. Wang, X. Feng, K. Müllen, *Chem. Soc. Rev.* **2015**, *44*, 6616.
[9] G. M. Beneventi, M. Krug, D. Reger, N. Jux, D. M. Guldi, *J. Photochem. Photobiol. C Photochem. Rev.* **2023**, *56*, 100602.
[10] R. Rieger, K. F. Y. Müllen, *J. Phys. Org. Chem.* **2010**, *23*, 315.
[11] R. K. Dubey, M. Marongiu, S. Fu, G. Wen, M. Bonn, H. I. Wang, M. Melle-Franco, A. Mateo-Alonso, *Chem* **2023**, *9*, 2983.
[12] X. Wang, J. Ma, W. Zheng, S. Osella, N. Arisnabarreta, J. Droste, G. Serra, O. Ivasenko, A. Lucotti, D. Beljonne, M. Bonn, X. Liu, M. R. Hansen, M. Tommasini, S. De Feyter, J. Liu, H. I. Wang, X. Feng, *J. Am. Chem. Soc.* **2022**, *144*, 228.
[13] W. Niu, J. Ma, P. Soltani, W. Zheng, F. Liu, A. A. Popov, J. J. Weigand, H. Komber, E. Poliani, C. Casiraghi, J. Droste, M. R. Hansen, S. Osella, D. Beljonne, M. Bonn, H. I. Wang, X. Feng, J. Liu, Y. Mai, *J. Am. Chem. Soc.* **2020**, *142*, 18293.
[14] E. Di Donato, M. Tommasini, G. Fustella, L. Brambilla, C. Castiglioni, G. Zerbi, C. D. Simpson, K. Müllen, F. Negri, *Chem. Phys.* **2004**, *301*, 81.
[15] M. Müller, V. S. Iyer, C. Kübel, V. Enkelmann, K. Müllen, *Angew. Chem. Int. Ed. Engl.* **1997**, *36*, 1607.
[16] J. Cai, P. Ruffieux, R. Jaafar, M. Bieri, T. Braun, S. Blankenburg, M. Muoth, A. P. Seitsonen, M. Saleh, X. Feng, K. Müllen, R. Fasel, *Nature* **2010**, *466*, 470.
[17] M. Treier, C. A. Pignedoli, T. Laino, R. Rieger, K. Müllen, D. Passerone, R. Fasel, *Nat. Chem.* **2011**, *3*, 61.
[18] A. Halleux, R. H. Martin, G. S. D. King, *Helv. Chim. Acta* **1958**, *41*, 1177.
[19] E. Clar, C. T. Ironside, M. Zander, *J. Chem. Soc. Resumed* **1959**, 142.
[20] W. Hendel, Z. H. Khan, W. Schmidt, *Tetrahedron* **1986**, *42*, 1127.
[21] A. Stabel, P. Herwig, K. Müllen, J. P. Rabe, *Angew. Chem. Int. Ed. Engl.* **1995**, *34*, 1609.
[22] Y. Li, Y. Hu, Y. Zhao, G. Shi, L. Deng, Y. Hou, L. Qu, *Adv. Mater.* **2011**, *23*, 776.
[23] F. Liu, M.-H. Jang, H. D. Ha, J.-H. Kim, Y.-H. Cho, T. S. F. Seo, *Adv. Mater.* **2013**, *25*, 3657.
[24] J. Ge, M. Lan, B. Zhou, W. Liu, L. Guo, H. Wang, Q. Jia, G. Niu, X. Huang, H. Zhou, X. Meng, P. Wang, C.-S. Lee, W. Zhang, X. Han, *Nat. Commun.* **2014**, *5*, 4596.
[25] Y. Cui, L. Liu, M. Shi, Y. Wang, X. Meng, Y. Chen, Q. Huang, C. Liu, *C J. Carb. Res.* **2024**, *10*, 7.
[26] Y. Huang, F. Xu, L. Ganzer, F. V. A. Camargo, T. Nagahara, J. Teyssandier, H. Van Gorp, K. Basse, L. A. Straasø, V. Nagyte, C. Casiraghi, M. R. Hansen, S. De Feyter, D. Yan, K. Müllen, X. Feng, G. Cerullo, Y. Mai, *J. Am. Chem. Soc.* **2018**, *140*, 10416.
[27] A. Tries, S. Osella, P. Zhang, F. Xu, C. Ramanan, M. Kläui, Y. Mai, D. Beljonne, H. I. Wang, *Nano Lett.* **2020**, *20*, 2993.
[28] T. Nagahara, F. V. A. Camargo, F. Xu, L. Ganzer, M. Russo, P. Zhang, A. Perri, G. de la Cruz Valbuena, I. A. Heisler, C. D'Andrea, D. Polli, K. Müllen, X. Feng, Y. Mai, G. Cerullo, *Nano Lett.* **2024**, *24*, 797.
[29] M. G. Debije, J. Piris, M. P. de Haas, J. M. Warman, Ž. Tomović, C. D. Simpson, M. D. Watson, K. Müllen, *J. Am. Chem. Soc.* **2004**, *126*, 4641.
[30] A. M. van de Craats, J. M. Warman, K. Müllen, Y. Geerts, J. D. Brand, *Adv. Mater.* **1998**, *10*, 36.

[31] L. Schmidt-Mende, A. Fechtenkötter, K. Müllen, E. Moons, R. H. Friend, J. D. MacKenzie, *Science* **2001**, *293*, 1119.
[32] J. P. Hill, W. Jin, A. Kosaka, T. Fukushima, H. Ichihara, T. Shimomura, K. Ito, T. Hashizume, N. Ishii, T. Aida, *Science* **2004**, *304*, 1481.
[33] W. Zhang, W. Jin, T. Fukushima, A. Saeki, S. Seki, T. Aida, *Science* **2011**, *334*, 340.
[34] Y. Yamamoto, G. Zhang, W. Jin, T. Fukushima, N. Ishii, A. Saeki, S. Seki, S. Tagawa, T. Minari, K. Tsukagoshi, T. Aida, *Proc. Natl. Acad. Sci. USA* **2009**, *106*, 21051.
[35] T. Aida, E. W. Meijer, S. I. Stupp, *Science* **2012**, *335*, 813.
[36] H. M. Jeong, J. W. Lee, W. H. Shin, Y. J. Choi, H. J. Shin, J. K. Kang, J. W. Choi, *Nano Lett.* **2011**, *11*, 2472.
[37] C. Bie, H. Yu, B. Cheng, W. Ho, J. Fan, J. D. Yu, *Adv. Mater.* **2021**, *33*, 2003521.
[38] R. E. Blackwell, F. Zhao, E. Brooks, J. Zhu, I. Piskun, S. Wang, A. Delgado, Y.-L. Lee, S. G. Louie, F. R. Fischer, *Nature* **2021**, *600*, 647.
[39] X.-Y. Wang, X. Yao, A. Narita, K. Müllen, *Acc. Chem. Res.* **2019**, *52*, 2491.
[40] X.-Y. Wang, M. Richter, Y. He, J. Björk, A. Riss, R. Rajesh, M. Garnica, F. Hennersdorf, J. J. Weigand, A. Narita, R. Berger, X. Feng, W. Auwärter, J. V. Barth, C.-A. Palma, K. Müllen, *Nat. Commun.* **2017**, *8*, 1948.
[41] Q. Liu, B. Guo, Z. Rao, B. Zhang, J. R. Gong, *Nano Lett.* **2013**, *13*, 2436.
[42] Y. Li, Y. Zhao, H. Cheng, Y. Hu, G. Shi, L. Dai, L. Qu, *J. Am. Chem. Soc.* **2012**, *134*, 15.
[43] S. Bhattacharyya, F. Ehrat, P. Urban, R. Teves, R. Wyrwich, M. Döblinger, J. Feldmann, A. S. Urban, J. K. Stolarczyk, *Nat. Commun.* **2017**, *8*, 1401.
[44] J. Fang, Y. Wang, M. Kurashvili, S. Rieger, W. Kasprzyk, Q. Wang, J. K. Stolarczyk, J. Feldmann, T. Debnath, *Angew. Chem., Int. Ed.* **2023**, *62*, e202305817.
[45] Z. Li, Y. Bu, S. Xie, Y. Ni, K. Yang, Z. Zeng, *Chem. Mater.* **2024**, *36*, 3058.
[46] M. C. Drummer, V. Singh, N. Gupta, J. L. Gesiorski, R. B. Weerasooriya, K. D. Glusac, *Photosynth. Res.* **2021**, *151*, 163.
[47] D. Medina-Lopez, T. Liu, S. Osella, H. Levy-Falk, N. Rolland, C. Elias, G. Huber, P. Ticku, L. Rondin, B. Jousselme, D. Beljonne, J.-S. Lauret, S. Campidelli, *Nat. Commun.* **2023**, *14*, 4728.
[48] V. Singh, M. R. Zoric, G. N. Hargenrader, A. J. S. Valentine, O. Zivojinovic, D. R. Milic, X. Li, K. D. Glusac, *J. Phys. Chem. Lett.* **2020**, *11*, 210.
[49] P. Haines, R. Kaur, M. M. Martin, M. B. Minameyer, S. Frühwald, S. Bönisch, D. Lungerich, F. Hampel, A. Görling, T. Drewello, N. Jux, D. M. Guldi, *Adv. Energy Mater.* **2021**, *11*, 2100158.
[50] T. Umeyama, T. Hanaoka, H. Yamada, Y. Namura, S. Mizuno, T. Ohara, J. Baek, J. Park, Y. Takano, K. Stranius, N. V. Tkachenko, H. Imahori, *Chem. Sci.* **2019**, *10*, 6642.
[51] M. Wolf, D. Lungerich, S. Bauroth, M. Popp, B. Platzer, T. Clark, H. L. Anderson, N. Jux, D. M. Guldi, *Chem. Sci.* **2020**, *11*, 7123.
[52] Q. Chen, L. Brambilla, L. Daukiya, K. S. Mali, S. De Feyter, M. Tommasini, K. Müllen, A. Narita, *Angew. Chem., Int. Ed.* **2018**, *57*, 11233.
[53] S. Garcia-Orrit, V. Vega-Mayoral, Q. Chen, G. Serra, G. M. Paternò, E. Cánovas, A. Narita, K. Müllen, M. Tommasini, J. Cabanillas-González, *Small* **2023**, *19*, 2301596.
[54] Q. Chen, A. Lodi, H. Zhang, A. Gee, H. I. Wang, F. Kong, M. Clarke, M. Edmondson, J. Hart, J. N. O'Shea, W. Stawski, J. Baugh, A. Narita, A. Saywell, M. Bonn, K. Müllen, L. Bogani, H. L. Anderson, *Nat. Chem.* **2024**, https://doi.org/10.1038/s41557-024-01477-1.
[55] Y.-C. Cheng, G. R. Fleming, *Annu. Rev. Phys. Chem.* **2009**, *60*, 241.
[56] I. McConnell, G. Li, G. W. Brudvig, *Chem. Biol.* **2010**, *17*, 434.
[57] J. E. Yarnell, J. C. Deaton, C. E. McCusker, F. N. Castellano, *Inorg. Chem.* **2011**, *50*, 7820.
[58] A. Quaranta, G. Charalambidis, C. Herrero, S. Margiola, W. Leibl, A. Coutsolelos, A. Aukauloo, *Phys. Chem. Chem. Phys.* **2015**, *17*, 24166.
[59] Z. Jin, S. Qi, X. Guo, N. Tian, Y. Hou, C. Li, X. Wang, Q. Zhou, *Chem. Commun.* **2020**, *56*, 2845.
[60] R. Canton-Vitoria, T. Scharl, A. Stergiou, A. Cadranel, R. Arenal, D. M. Guldi, N. Tagmatarchis, *Angew. Chem., Int. Ed.* **2020**, *59*, 3976.
[61] L. Chai, Y.-Y. Ju, J.-F. Xing, X.-H. Ma, X.-J. Zhao, Y.-Z. Tan, *Angew. Int. Ed. Chem.* **2022**, *61*, 202210268.
[62] H. Noguchi, K. Hojo, M. Suginome, *J. Am. Chem. Soc.* **2007**, *129*, 758.
[63] H. Noguchi, T. Shioda, C.-M. Chou, M. Suginome, *Org. Lett.* **2008**, *10*, 377.
[64] D. Reger, K. Schöll, F. Hampel, H. Maid, N. Jux, *Chem. – Eur. J.* **2021**, *27*, 1984.
[65] H. Yoshida, Y. Takemoto, K. Takaki, *Chem. Commun.* **2015**, *51*, 6297.
[66] X. Yang, X. Dou, K. Müllen, *Chem. – Asian J.* **2008**, *3*, 759.
[67] M. Tsutsui, D. Ostfeld, L. M. Hoffman, *J. Am. Chem. Soc.* **1971**, *93*, 1820.
[68] L. Chai, J.-H. Li, H.-Z. Fang, J.-F. Xing, X.-H. Ma, X.-J. Zhao, Y. Yang, Y.-Z. Tan, *J. Organomet. Chem.* **2023**, *1001*, 122877.
[69] L. Goerigk, S. Grimme, *J. Chem. Theory Comput.* **2011**, *7*, 3272.
[70] S. K. Behera, S. Y. Park, J. Gierschner, *Angew. Chem., Int. Ed.* **2021**, *60*, 22624.
[71] T. Itoh, *Chem. Rev.* **2012**, *112*, 4541.
[72] D. G. Hager, G. A. Crosby, *J. Am. Chem. Soc.* **1975**, *97*, 7031.
[73] P. Haines, D. Reger, J. Träg, V. Strauss, D. Lungerich, D. Zahn, N. Jux, D. M. Guldi, *J. Nanoscale* **2021**, *13*, 801.
[74] P. Ceroni, V. Balzani, A. Juris, *Photochemistry and Photophysics*, Wiley-VCH, Weinheim **2014**.
[75] I. Iwakura, A. Yabushita, T. Kobayashi, *Eur. J. Inorg. Chem.* **2008**, *2008*, 4856.
[76] D. P. Rillema, J. K. Nagle, L. F. Barringer Jr., T. J. Meyer, *J. Am. Chem. Soc.* **1981**, *103*, 56.
[77] A. Prodi, M. T. Indelli, C. J. Kleverlaan, F. Scandola, E. Alessio, T. Gianferrara, L. G. Marzilli, *Chem. – Eur. J.* **1999**, *5*, 4856.
[78] D. M. Roundhill, *Photochemistry In Photochemistry and Photophysics of Metal Complexes, Modern Inorganic Chemistry*, Springer US, Boston, MA **1994**, pp. 321–340.
[79] G. W. Sovocool, F. R. Hopf, D. G. Whitten, *J. Am. Chem. Soc.* **1972**, *94*, 4350.
[80] K. Ishii, S. I. Hoshino, N. Kobayashi, *Inorg. Chem.* **2004**, *43*, 7969.
[81] G. W. Sovocool, F. R. Hopf, D. G. Whitten, *J. Am. Chem. Soc.* **1972**, *94*, 4350.
[82] Y. Gao, V. Walter, M. J. Ferguson, R. R. Tykwinski, *Chem. – Eur. J.* **2020**, *26*, 16712.
[83] G. Soavi, S. Dal Conte, C. Manzoni, D. Viola, A. Narita, Y. Hu, X. Feng, U. Hohenester, E. Molinari, D. Prezzi, K. Müllen, G. Cerullo, *Nat. Commun.* **2016**, *7*, 11010.
[84] G. M. Paternò, Q. Chen, X.-Y. Wang, J. Liu, S. G. Motti, A. Petrozza, X. Feng, G. Lanzani, K. Müllen, A. Narita, F. Scotognella, *Angew. Chem., Int. Ed.* **2017**, *56*, 6753.
[85] It decays in 26 ns to the ground state, in parallel to the other two states. Its GSB minima are blue-shifted with respect to those recorded for **RuP-2-RuP**, in agreement with the steady-state measurements. It was impossible to deconvolute such state in the fs-TAS experiments, as its lifetime is much longer than the time window of our experiments. Furthermore, due to its weak intensity, we were unable to deconvolute ($T_1$) of monomeric **2** from that of **RuP-2-RuP**.
[86] I. H. M. van Stokkum, D. S. Larsen, R. van Grondelle, *Biochim. Biophys. Acta – Bioenerg.* **2004**, *1657*, 82.
[87] J. J. Snellenburg, S. Laptenok, R. Seger, K. M. Mullen, I. H. M. van Stokkum, *J. Stat. Softw.* **2012**, *49*, 1.
[88] K. M. Mullen, I. H. M. van Stokkum, *J. Stat. Softw.* **2007**, *18*, 1.